Journal of Materials Chemistry A

Accepted Manuscript

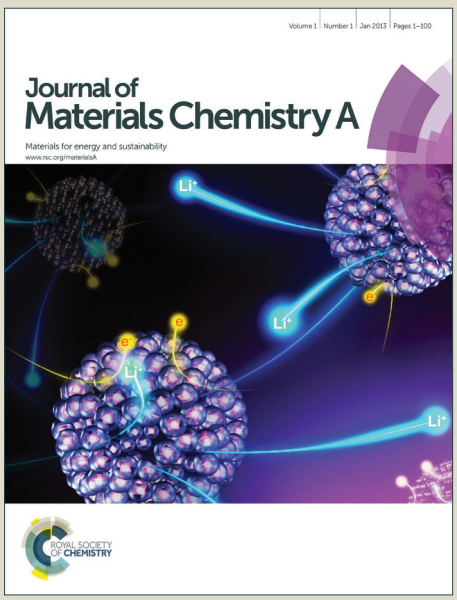

ROYAL SOCIETY OF CHEMISTRY

www.rsc.org/materialsA

Direct Growth of Porous Crystalline $NiCo_2O_4$ Nanowire Arrays on Conductive Electrode for High-Performance Electrocatalytic Water Oxidation

Xingxing Yu, Zijun Sun, Zhiping Yan, Bin Xiang,* Xiang Liu, and Pingwu Du*

CAS Key Laboratory of Materials for Energy Conversion, Department of Materials Science and Engineering, and the Collaborative Innovation Center of Chemistry for Energy Materials (*i*ChEM), University of Science and Technology of China, Hefei, China 230026

*Corresponding author: dupingwu@ustc.edu.cn, binxiang@ustc.edu.cn
Tel/Fax: 86-551-63606207

Abstract: Herein we report a facile and direct synthesis of porous $NiCo_2O_4$ nanowire arrays (NWAs) with robust mechanical adhesion to conductive electrodes by a simple two-step method. Upon complete pyrolysis of the cobalt-nickel-hydroxide precursor, high-quality crystalline $NiCo_2O_4$ is achieved. The porous $NiCo_2O_4$ nanowires were found to be highly active for catalytic water oxidation when serving as the working electrodes without any external materials (binder *and/or* carbon black), as evidenced by exhibiting higher catalytic current density for water oxidation compared to precious metal oxide catalysts such as iridium oxide (IrO_2) under the same conditions and appreciable catalytic wave at ~1.52 V (vs. RHE). The optimal performance of the as-synthesized $NiCo_2O_4$ nanowires showed a current density of 10 mA/cm^2 under an overpotential of only 0.46 V and 20 mA/cm^2 under an overpotential of 0.72 V, corresponding to a Faradaic efficiency of nearly 100%. The atomic-scale analysis of the $NiCo_2O_4$ nanowires was further conducted by spherical-aberration-corrected transmission electron microscopy (TEM). The highly exposed high-index facets and one-dimensional (1D) configuration of the as-synthesized porous $NiCo_2O_4$ nanowires may be responsible for the high catalytic performance of water oxidation, which exhibits excellent activity and unique advantages for catalytic water splitting.

Keywords: noble-metal-free electrocatalyst, water oxidation, nanowire arrays, porous structure, water splitting

Introduction

Hydrogen is considered to be a sustainable, carbon-neutral and abundant energy carrier with potential to solve the current energy problem.[1-4] Electrocatalytic/photocatalytic water splitting to produce hydrogen and oxygen, as a means of providing a clean and renewable energy source, has been studied for more than four decades.[1,5-12] It is considered that the water oxidation reaction is more difficult than water reduction reaction because the former proceeds a process of four electrons coupled with four protons during water splitting.[13-14] However, the highly active electrocatalysts for water oxidation are mostly from noble metals such as RuO_2[7,15] and IrO_2.[16] These electrocatalysts are scarce and expensive to use in constructing artificial photosynthetic systems that store and utilize solar energy.[13,17-18] Thus, it is important to develop low-cost and abundant materials as catalysts with high efficiency for the water oxidation reaction.[9,11,19]

Nature uses a $CaMn_4O_x$ cluster for the oxidation of water in photosystem II.[20-22] To simulate the function of $CaMn_4O_x$ and explore abundant catalysts for water oxidation, various manganese oxides or complexes have been well studied.[17-18,23-25] Recently, attention has transferred to developing abundant catalysts made of cobalt,[6,9,26-30] nickel,[1,3,31] copper,[32] and iron oxides[33-34] to reduce the cost and enhance the efficiency of catalysts for water oxidation.

Amongst them, considerable interest has been focused on cobalt related spinel structures, generally $M_xCo_{3-x}O_4$ materials (M = Mn, Ni, Fe, Zn).[19,35-39] These catalysts show great potentials in possible applications for their advantages of low-cost, abundance, good stability, and high efficiency. Highly improved performance in

cobalt oxide spinels was found by nickel substitution for electrocatalytic water oxidation.[40-41]

Herein we report facile synthesis and atomic-scale analysis of porous crystalline $NiCo_2O_4$ nanowire arrays (NWAs) as a highly active electrocatalyst for the oxygen evolution reaction (OER). High-index facets were found by spherical-aberration-corrected transmission electron microscopy (TEM). The $NiCo_2O_4$ NWAs catalyst can be grown directly on conductive fluorine doped tin oxide (FTO) electrode, exhibiting quite low overpotential and very high catalytic current densities. The variation in the morphologies of as-synthesized cobalt-nickel hydroxide, resulting from the hydrothermal time, leads to distinguishable electrochemical performance. To probe the mechanism of the electrochemical performance, atomic-scale analysis of as-synthesized cobalt-nickel hydroxide was carried out by the spherical-aberration-corrected TEM.

Experimental

***Materials**:* All reagents, including nickel nitrate hexahydrate ($Ni(NO_3)_2{\cdot}6H_2O$, 99%), cobalt nitrate hexahydrate ($Co(NO_3)_2{\cdot}6H_2O$, 99%), urea (98%), ammonium fluoride (NH_4F, 98%), 5 wt% Nafion solution, potassium hydroxide (KOH), and ethanol were purchased from Aldrich or Acros. Iridium oxide nanoparticles (IrO_2, 99%) was purchased from Shanxi Kaida Chemical Engineering Co. LTD. All the aqueous solutions involved in the paper were freshly prepared. Fluorine-doped tin oxide (FTO) glass plates with surface resistivity of 8-10 Ω/sq were purchased from Zhuhai Kaivo

Electronic Components Co., Ltd. Prior to the tests, FTO electrodes were successively ultrasonicated in deionized water, ethanol, and deionized water for 5 minutes and dried in air.

Synthesis of $NiCo_2O_4$ nanoflakes and nanowire arrays: Highly porous $NiCo_2O_4$ nanoflakes and nanowire arrays were directly synthesized on an FTO glass plate by a mild hydrothermal method. Details of the procedures used are as follows: 0.5 mmol of $Ni(NO_3)_2{\cdot}6H_2O$, 1 mmol of $Co(NO_3)_2{\cdot}6H_2O$, 3 mmol of NH_4F, 7.5 mmol of urea were dissolved in 30 ml of deionized water. After stirring for 30 min, a light pink-colored aqueous solution was obtained, then the resulting solution was transferred into a 50 mL Teflon-lined stainless steel autoclave with the clean FTO glass plates immersed into the solution. The autoclave was heated to 120 ºC and the temperature was maintained for different times to obtain various morphologies. After cooling to room temperature, the pink precursor on FTO was washed with deionized water for three times. Then the cobalt-nickel hydroxide precursors were transferred to a tube furnace and calcinated at 350 ºC for 2 hours under flowing argon, after which the resulting plates were used as the working electrodes in electrochemical experiments.

Cyclic voltammetry (CV): All electrochemical CV experiments were performed at room temperature with a CHI660D Instrument Potentialstat (purchased from Shanghai Chen Hua Instrument Co., Ltd.). In a typical three-electrode electrochemical system, the $NiCo_2O_4$ nanoflakes or nanowires or nanosized IrO_2 on FTO glass plates were used as the working electrodes, an Ag/AgCl electrode (3 M KCl) as reference electrode, and a platinum wire as counter electrode to obtain cyclic voltammograms.

The electrolyte solutions were 0.1 M KOH or 1 M KOH aqueous solution and all the potentials reported in this paper were versus RHE (reversible hydrogen electrode), with the potential of RHE defined as E_{RHE} = -0.059pH. Hence the potentials in solution are according to the formula: $E = E_{applied} + E_{Ag/AgCl} + 0.059pH$, where $E_{applied}$ is the applied potential vs Ag/AgCl and $E_{Ag/AgCl}$ =0.21 V in 3 M KCl.[42] All the cyclic voltammograms were measured at 5 mV/s. There were *iR* compensations and no stirring for the CV tests.

Bulk electrolysis and chronopotentiometry*:* The $NiCo_2O_4$ nanoflakes and nanowires on FTO glass plates were used as the working electrodes in a 40 mL 0.1 M or 1 M KOH aqueous solution for bulk electrolysis ($E_{applied}$ =0.8 V). For chronopotentiometry, the $NiCo_2O_4$ nanowires on FTO plates were used as the working electrode with a fixed current density of 10 mA/cm^2 or 20 mA/cm^2 in a 40 mL 1 M KOH solution. For comparison, the IrO_2 catalyst mixed with Nafion and ethonal was dropped onto the FTO plates as the working electrode and all other conditions are the same as those for $NiCo_2O_4$ nanowires.

Tafel plot*:* The Tafel plot was obtained by performing bulk electrolysis in solution at a variety of anodic potentials until a steady current density was achieved. The potentials were varied from 1.24 V to 2.54 V and the intervals were 50 mV or 25 mV for each test. Prior to the experiment, the solution resistance was measured using the *iR* function.

The Faradaic efficiency*:* A fluorescence-based oxygen sensor (Ocean Optics) was used for quantitative detection of O_2. The experiment was performed in a gas-tight

electrochemical cell. The solution of 1 M KOH was degassed by bubbling with high purity N_2 for 20 minutes with vigorous stirring. The reference electrode was positioned 3-5 millimeter from the $NiCo_2O_4$ working electrode. The O_2 on the FOXY probe, recorded at 2s intervals, was converted into the partial pressure of O_2 in the headspace. After calibration, bulk electrolysis was initiated at 1.83 V vs. RHE.

X-ray diffraction (XRD)*:* The crystal phase analysis of the $NiCo_2O_4$ electrocatalysts and the $NiCo_2O_4$ nanowires after bulk electrolysis at 1.78 V in 0.1 M KOH or 1.83 V in 1 M KOH was measured by X-ray diffraction (XRD, D/max-TTR III) via graphite monochromatized Cu Ka radiation of 1.5417 Å, operating at 40 kV and 200 mA. The scanning rate was 5˚ min^{-1} from 10˚ to 70˚ in 2θ.

Scanning electron microscopy (SEM) and transmission electron microscopy (TEM)*:* SEM images were obtained with a SIRION200 Schottky field emission scanning electron microscope (SFE-SEM). The detected $NiCo_2O_4$ nanowires on FTO plate were coated with Pt to make the samples conductive before loading into the instrument. Images were obtained with an acceleration voltage of 5 kV or 10 kV. The morphologies of $NiCo_2O_4$ samples were further analyzed by TEM. TEM images were obtained on a JEM-2011 electron microscope, operated at an acceleration voltage of 200 kV.

High resolution transmission electron microscopy (HRTEM), electron diffraction (ED), and energy-dispersive X-ray analysis (EDX)*:* The morphologies of the $NiCo_2O_4$ nanowires were also determined by high-resolution transmission electron microscopy (HRTEM) equipped with an electron diffraction (ED) attachment with an

acceleration voltage of 200 kV, and equipped with a Rontec EDX system.

X-ray photoelectron spectroscopy (XPS)*:* The elemental composition of the $NiCo_2O_4$ samples on FTO plates and the valence states of the metal elements were probed with the ESCALAB 250 X-ray photoelectron spectroscopy (XPS) instrument. The survey scan, high resolution Co 2p, and high resolution Ni 2p spectra were obtained. The spectra are referenced to the C 1s peak (285.0 eV).

Facet notation for high Miller index surfaces*:* For a fcc crystal, a high Miller index (hkl) of a surface with ($h_tk_tl_t$) terraces, ($h_sk_sl_s$) steps, and a step-to-terrace atom ratio of $n^{uc}_{h_tk_tl_t}$:$n^{uc}_{h_sk_sl_s}$ can be written as:[43]

$$(hkl) = \frac{n^{uc}_{h_tk_tl_t}}{P_t}(h_tk_tl_t) + \frac{n^{uc}_{h_sk_sl_s}}{P_s}(h_sk_sl_s)$$

Where h_t, k_t, l_t, must be an irreducible set of integers; h_s, k_s, l_s must also be an irreducible set of integers. P_t=4 as h_t, k_t, l_t are all odd; P_t=2 as h_t, k_t, l_t are not all odd. P_s=4 as h_s, k_s, l_s are all odd; P_s=2 as h_s, k_s, l_s are not all odd. Therefore, we are able to identify the curved surfaces as long as we have the terrace and step facet information.

Results and discussion

The two-step synthetic process of porous $NiCo_2O_4$ nanowire arrays (NWAs) on fluorine-doped tin oxide (FTO) started from a hydrothermal process at 120 ºC for a certain time (2-15 hours), followed by calcining at 350 ºC in flowing argon for 2 hours. Figure 1 shows the scanning electron microscopy (SEM) images of the as-synthesized $NiCo_2O_4$ on FTO. After 10 hours of the hydrothermal process, the image showed a large number of $NiCo_2O_4$ nanowires with a mean diameter of ~70

nm, as calculated from 30 nanowires randomly selected from the SEM images (Figure 1a-b). The lengths of the nanowires varied from 2-5 micrometers. The thickness of the nanowires is 3-4 μM on FTO (Figure 1c). The morphologies of $NiCo_2O_4$ can be controlled by the operation time for the hydrothermal process, as shown in Figure S1. After 2 hours of the hydrothermal process, the materials show obvious nanoflake structures. As the hydrothermal process continues, nanowires gradually grow during the crystallization process. The morphology of $NiCo_2O_4$ after 4 hours of hydrothermal process clearly exhibits this transition process from nanoflakes to nanowires (Figure S1b). The morphologies show more nanowires on FTO after a longer hydrothermal time (Figure 1c-e). The elements of Ni and Co in nanowires of $NiCo_2O_4$ were investigated by energy dispersive X-ray spectroscopy (EDX) analysis (Figure S2). The results show the elemental molar concentrations of Ni and Co in $NiCo_2O_4$ nanowires are 10.83% and 23.64%, corresponding to a ~1:2 atomic ratio of Ni:Co. The elemental Cu is from the copper substrate.

Figure 1d shows the X-ray diffraction (XRD) patterns of the nanowires. All the synthesized samples exhibit very similar diffraction features. The peaks at 2θ = 31.1, 36.5, 44.6, 59.1, and 64.9 ° correspond to the diffractions from the (220), (311), (400), (511), and (440) planes of spinel $NiCo_2O_4$ (JCPDS card no. 73-1702). No other peaks were observed in the X-ray diffraction pattern, indicating the pure-phase nature of the nanowires.

In addition, the $NiCo_2O_4$ nanowires on FTO substrate were analyzed by X-ray photoelectron spectroscopy (XPS) (Figure 2). The XPS spectra indicate the presence

of Ni, Co, and O elements (Figure 2a), consistent with the results obtained by EDX. The XPS analysis of $NiCo_2O_4$ shows that the surface composition percentages of Ni, Co and O are 11.1%, 15.2% and 43.6%, indicating that Ni is enriched on the surface of $NiCo_2O_4$ nanowires. The high resolution Ni 2p and Co 2p XPS peaks are shown in Figure 2b and 2c. In Ni 2p spectra, two sets of broad signals corresponding to Ni $2p_{3/2}$ (855.4 eV) and Ni $2p_{1/2}$ (872.9 eV) are observed, showing that the elemental Ni is in a range of typical Ni^{2+} or Ni^{3+} bound to oxygen.[44] The intense satellite peaks indicate that the majority of nickel elements in the crystal lattice are Ni^{2+} cations.[45] In Co 2p region of the sample, two sets of broad signals consistent with Co $2p_{3/2}$ (779.8 eV) and Co $2p_{1/2}$ (794.9 eV) are observed, implying a fundamental oxidation state of Co^{3+} ions in $NiCo_2O_4$ nanowires.[42,45-47] The O 1s signal is located at 529.4 eV and 531.1 eV, showing that the peak at 529.4 eV is typical of metal-oxygen bonds in $NiCo_2O_4$ nanowires (Figure 2d).[48] The spectra are referenced to the adventitious C 1s located at 285.0 eV. The results are consistent with the valence states of $NiCo_2O_4$ material.

The structural characteristics of the $NiCo_2O_4$ NWAs were further studied by transmission electron microscopy (TEM) and high resolution transmission electron microscopy (HRTEM). The TEM images (Figure 3a and 3b) confirm that the samples consist of $NiCo_2O_4$ nanowires and the average width of a single $NiCo_2O_4$ nanowire is ~70 nm. Obviously, large quantities of pore detects are distributed on the surface of $NiCo_2O_4$ nanowires (Figure S3, Figure 3a and 3b). Based on the XRD analysis, these nanowires were highly crystalline and showed good uniformity. Figure S4 shows the nitrogen adsorption-desorption isotherms measured at liquid nitrogen temperature.

The Brunauer-Emmett-Teller (BET) surface area is around 125.5 m^2/g, which is higher than previous reported results,[36,41] On the basis of selected-area electron diffraction (SAED) analysis (Figure 3c), these nanowires were consistently found to be single-crystalline. The set of diffraction spots can be indexed as (440), (220), and (400) facets. From the HRTEM image (Figure 3d), the spacing of the lattice fringes is calculated to be 2.45 Å and 2.87 Å, which can be indexed as the (311) and (220) planes of $NiCo_2O_4$ and is consistent with the diffraction peaks of the XRD patterns.

The success in controlling the growth of crystalline $NiCo_2O_4$ nanowires allowed systematic study of their catalytic performance. The electrocatalytic OER activity of the material was investigated in a standard three-electrode system in alkaline solutions. Besides giving good control over structural features, the direct synthesis of $NiCo_2O_4$ nanowires on conductive electrodes has several advantages over ex-situ catalyst film fabrication. For instance, it allows robust mechanical adhesion without an external binder and facilitates interfacial electron transfer between the catalysts and the electrodes, which could subsequently enhance the catalytic efficiency. Figure 4a shows the curves of cyclic voltammograms (CVs) and bulk electrolysis of the $NiCo_2O_4$ NWAs in a 1 M KOH solution. All the $NiCo_2O_4$ NWAs exhibit obvious catalytic currents at a potential > 1.52 V (vs. RHE, all the potentials in this paper are versus RHE). However, the $NiCo_2O_4$ flakes prepared with a hydrothermal process at 120 ºC for 2 hours show a much higher onset potential at > 1.65 V, indicating that the $NiCo_2O_4$ nanowires are more active for catalytic water oxidation than $NiCo_2O_4$ nanoflakes. The CVs data indicate that $NiCo_2O_4$ nanowires prepared with a

hydrothermal process at 120 ºC for 10 hours (~1.0 mg/cm^2 of the catalysts on FTO) have the best catalytic activity for catalytic water oxidation (Figure 4a). The catalytic current density is as high as ~47 mA/cm^2 with an overpotential of 1.0 V.

The apparent catalytic currents for water oxidation impelled us to examine bulk electrolysis catalyzed by the as-prepared $NiCo_2O_4$ NWAs. The catalytic water oxidation experiments were carried out with a fixed potential at 1.83 V (an overpotential of 0.60 V) in a 1 M KOH electrolyte, as shown in Figure 4b. The results exhibit that all the current densities using $NiCo_2O_4$ nanoflakes/nanowires are more than 10 mA/cm^2. Impressively, the $NiCo_2O_4$ nanowires prepared with a hydrothermal process at 120 ºC for 10 hours could achieve current densities as high as 16 mA/cm^2, which is a very high catalytic current density among those materials for water oxidation reported in the literature.[17,19,35,49] The catalytic activity has no significant decrease even after 4 hours of electrolysis. The results show that $NiCo_2O_4$ nanowires can effectively catalyze water oxidation in alkaline solutions.

Figure 4c-d shows the curves of cyclic voltammograms (CVs) and bulk electrolysis of the $NiCo_2O_4$ NWAs in a 0.1 M KOH solution. The $NiCo_2O_4$ NWAs exhibit the same tendency as the experiments run in a 1 M KOH solution, i.e. the $NiCo_2O_4$ nanowires are more active for catalytic water oxidation than $NiCo_2O_4$ nanoflakes. The $NiCo_2O_4$ nanowires prepared with a hydrothermal process at 120 ºC for 10 hours had the best activity (Figure 4c). At an applied overpotential of 0.94 V, the CV data show that catalytic current density could reach 20 mA/cm^2. Obvious catalytic currents were observed at an applied overpotential > 0.29 V for all $NiCo_2O_4$

nanowires. The catalytic current densities of bulk electrolysis at a fixed overpotential of 0.55 V show $NiCo_2O_4$ nanowires prepared with a hydrothermal process at 120 ºC for 10 hours could achieve > 6.5 mA/cm^2, and these activities showed no significant decrease even after 4 hours of electrolysis (Figure 4d). All the results of bulk electrolysis exhibited good durability of $NiCo_2O_4$ nanowires for efficient catalytic water oxidation in alkaline solutions.

For comparison, nanosized iridium oxide (IrO_2) catalyst (SEM image, see Figure S5) loaded on FTO electrode (~1.0 mg/cm^2 loading) was measured for catalytic water oxidation. In a 1 M KOH aqueous solution, the CV curves show that the $NiCo_2O_4$ nanowires perform much better than IrO_2 catalyst under the same conditions (Figure 5a). IrO_2 can catalyze water oxidation with a sharp onset overpotential of ~1.75 V, while the $NiCo_2O_4$ nanowires exhibit an onset overpotential of only ~1.52 V, which is ~0.23 V lower than the nanosized IrO_2 catalyst. The low performance of IrO_2 in the present study is probably due to ex-situ catalyst film fabrication.[49] It needs an external binder (for example, Nafion), which may result in worse contact between the catalyst and the electrode than the direct growth method in facilitating interfacial electron transfer. At a fixed potential, the current density of $NiCo_2O_4$ NWAs is much higher than IrO_2 catalyst under the same potential, confirming that $NiCo_2O_4$ nanowires catalyst is more active for water oxidation. The OER onset potential for the optimal $NiCo_2O_4$ nanowires was even lower than the performance of other reported OER catalysts in the literature, including Co_3O_4/N-graphene (1.63 V vs. RHE, pH 14),[50] $Mn_3O_4/CoSe_2$ catalyst (1.68 V vs. RHE, pH 13),[51] $Ni_xCo_{3-x}O_4$ catalyst (1.62 V vs.

RHE, pH 14, table S1),[41] $Zn_xCo_{3-x}O_4$ catalyst (1.55 V vs. RHE, pH 14, table S1),[36] Nitrogen doped graphene-$Ni_xCo_{3-x}O_4$ catalyst (1.54 V vs. RHE, pH 14, table S1),[40] N/C–NiO_x catalyst (1.7 V vs. RHE, pH 13),[49] and the metal free N/C nanomaterials.[49] Therefore, the present $NiCo_2O_4$ nanowires electrocatalyst is among the known highly active non-precious metal oxide or mixed metal oxide electrocatalysts in alkaline solutions.

The chronopotentiometric curves of the $NiCo_2O_4$ nanowires and the IrO_2 catalyst under current densities of 10 and 20 mA/cm^2 for water oxidation were further investigated (Figure 5b). The results show that the required overpotential of $NiCo_2O_4$ nanowires under current density of 20 mA/cm^2 is ~0.72 V, while the potentials of IrO_2 under same current density requires ~0.91 V, ~26% higher than $NiCo_2O_4$ nanowires. Similarly, for the current density of 10 mA/cm^2, the required overpotentials for $NiCo_2O_4$ nanowires and IrO_2 catalysts are ~0.54 V and ~0.63 V, respectively. The chronopotentiometric data also confirm great stability and high activity of the as-synthesized $NiCo_2O_4$ nanowires during catalytic water oxidation reaction. The turnover frequencies (TOFs) are 0.0028 s^{-1} and 0.0047 s^{-1} for $NiCo_2O_4$ nanoflakes and nanowires, respectively, under the overpotential of 0.55 V in 0.1 M KOH. Under the overpotential of 0.60 V in 1 M KOH, the TOFs are 0.0082 s^{-1} and 0.0123 s^{-1} for $NiCo_2O_4$ nanoflakes and nanowires, respectively. The result shows that the $NiCo_2O_4$ nanowires have better electrocatalytic activity than that of $NiCo_2O_4$ nanoflakes.

To investigate the mechanism of the high catalytic performance of the $NiCo_2O_4$ nanowires, spherical-aberration-corrected TEM were utilized to characterize the

microstructure of the material. Figure 6a and 6b reveal that the surface of the $NiCo_2O_4$ nanowires is composed of atomic steps. By indexing the rough features, high index $(4\bar{8}\bar{6})$ facets were observed on the surface of the $NiCo_2O_4$ nanowires. While the $NiCo_2O_4$ nanoflakes consist of smooth surfaces and there is no high index facet exposed on those smooth surfaces (Figure 6c and 6d). In general, the high index facet possesses high surface energy, resulting in instability when exposed to the surface of the crystal. However, the surface energy can be modified at atomic steps because of the irregularity, compared to perfect surface. As a result, the high index facets can be highly exposed to the surface in the presence of atomic steps.[52] In addition, the high density of atomic steps on the surface introduces new features in potential field, which in turn reduces the chemical reaction potential barriers. The adsorbant molecules can be feasibly decomposed at the surface with atomic steps as active sites while in the absence of the atomic steps, the decomposition reaction of the absorbant molecules has to meet the requirement of the potential barrier in chemical reactions. In terms of surface reactivity in OER, the high index facets provide more active sites for O-H chemical bond breaking and give rise to more catalytic active behavior.[53]

Tafel plot can show the electrochemical kinetics relating the rate of water oxidation reaction to the overpotential. The plot of current density vs potential was obtained by using $NiCo_2O_4$ nanowires prepared at 120 ºC for 10 hours as the working electrode in a 1 M KOH aqueous solution at a variety of the potentials (Figure 7a). When a steady current density was achieved, the potentials varied from 1.24 V to 2.54 V. The sharp onset potential of $NiCo_2O_4$ catalyst appears at ~1.52 V ($> 1 \times 10^{-4}$

mA/cm^2) and the slope of the line at higher potential is 90 mV per decade in a 1 M KOH solution, indicating that $NiCo_2O_4$ nanowires electrocatalyst is highly active for water oxidation.

The Faradaic efficiency of the $NiCo_2O_4$ nanowires catalyst was further measured by a fluorescence-based oxygen sensor. Bulk electrolysis was performed with an overpotential of 0.60 V in a 1 M KOH electrolyte in a gas-tight electrochemical cell under nitrogen. Oxygen bubbles were rapidly produced on the working electrode and the fluorescence sensor showed the rapid rise of the oxygen percentage in the headspace. The theoretical amount of oxygen evolution was calculated by assuming that the total charge was from 4e$^-$ oxidation of water according to Faraday's law. The amount of produced oxygen matched well with the theoretical amount of oxygen under the total charge during the process of the electrolysis, corresponding to a Faradaic efficiency of nearly 100% (Figure 7b).

In order to further confirm the stability of the catalyst during the OER, the structure and morphology of the $NiCo_2O_4$ nanowires catalyst was further examined by XRD and SEM. After a long process (> 10 hours) of bulk electrolysis in a 1 M KOH aqueous solution at an applied overpotential of 0.60 V, no significant difference in the morphology of the nanowires was observed before and after the bulk electrolysis (Figure 8a), presenting a very similar diameter of ~70 nm. After the catalysis, no significant changes of diffraction patterns could be detected by XRD measurement, indicating that the nanowires are not substantially dissolved into the solution from the FTO support (Figure 8b).

Conclusions

In conclusion, we utilized a simple two-step method to synthesize porous crystalline $NiCo_2O_4$ NWAs on FTO substrates as a highly active electrocatalyst for catalytic water oxidation. The $NiCo_2O_4$ NWAs catalyst exhibits quite low overpotential and high activity, which is comparable to the nanosized IrO_2 catalyst and other reported non-precious metal-based water oxidation catalysts under the same condition. A Faradaic efficiency of nearly 100% for water oxidation was achieved in the present system. In addition, great structural and chemical stability was observed during the catalytic water oxidation reaction. The atomic-scale analysis of the $NiCo_2O_4$ nanowires was conducted by spherical-aberration-corrected TEM. The high density of surface atomic steps in the present $NiCo_2O_4$ nanowires could contribute to the low overpotential and high catalytic activity for water oxidation. Therefore, we believe that the direct synthesis of crystalline $NiCo_2O_4$ NWAs on conductive electrodes represents a good approach to preparing an electrocatalyst for high-performance catalytic water oxidation without precious metals.

Acknowledgements

This work was financially supported by the National Natural Science Foundation of China (21271166 and 21473170 for P.D., 21373196 for B.X.), the Fundamental Research Funds for the Central Universities (WK2060140015, WK2060190026), the Program for New Century Excellent Talents in University (NCET), and the Thousand

Young Talents Program.

Supporting Information.

Additional characterization data and figures: SEM and TEM images, EDX data, and BET data. This information is available free of charge via the Internet at http://pubs.rsc.org/.

References

(1) Bediako, D. K.; Lassalle-Kaiser, B.; Surendranath, Y.; Yano, J.; Yachandra, V. K.; Nocera, D. G. *J. Am. Chem. Soc.* **2012**, *134*, 6801-6809.
(2) Gao, M. R.; Cao, X.; Gao, Q.; Xu, Y. F.; Zheng, Y. R.; Jiang, J.; Yu, S. H. *ACS Nano* **2014**, *8*, 3970-3978.
(3) Bediako, D. K.; Costentin, C.; Jones, E. C.; Nocera, D. G.; Saveant, J. M. *J. Am. Chem. Soc.* **2013**, *135*, 10492-10502.
(4) Louie, M. W.; Bell, A. T. *J. Am. Chem. Soc.* **2013**, *135*, 12329-12337.
(5) Dempsey, J. L.; Brunschwig, B. S.; Winkler, J. R.; Gray, H. B. *Acc. Chem. Res.* **2009**, *42*, 1995-2004.
(6) Gerken, J. B.; McAlpin, J. G.; Chen, J. Y. C.; Rigsby, M. L.; Casey, W. H.; Britt, R. D.; Stahl, S. S. *J. Am. Chem. Soc.* **2011**, *133*, 14431-14442.
(7) Meyer, T. J.; Huynh, M. H. V. *Inorg. Chem.* **2003**, *42*, 8140-8160.
(8) Cao, R.; Lai, W.; Du, P. *Energy Environ. Sci.* **2012**, *5*, 8134-8157.
(9) Du, P.; Eisenberg, R. *Energy Environ. Sci.* **2012**, *5*, 6012-6021.
(10) Duan, L.; Tong, L.; Xu, Y.; Sun, L. *Energy Environ. Sci.* **2011**, *4*, 3296-3313.
(11) Jiao, F.; Frei, H. *Energy Environ. Sci.* **2010**, *3*, 1018-1027.
(12) Lin, Y.; Yuan, G.; Sheehan, S.; Zhou, S.; Wang, D. *Energy Environ. Sci.* **2011**, *4*, 4862-4869.
(13) Bricker, T. M.; Roose, J. L.; Fagerlund, R. D.; Frankel, L. K.; Eaton-Rye, J. J. *Biochim. Biophys. Acta* **2012**, *1817*, 121-142.
(14) Han, A. L.; Wu, H. T.; Sun, Z. J.; Jia, H. X.; Du, P. W. *Phys. Chem. Chem. Phys.* **2013**, *15*, 12534-12538.
(15) Duan, L.; Bozoglian, F.; Mandal, S.; Stewart, B.; Privalov, T.; Llobet, A.; Sun, L. *Nat. Chem.* **2012**, *4*, 418-423.
(16) Zhao, Y. X.; Hernandez-Pagan, E. A.; Vargas-Barbosa, N. M.; Dysart, J. L.; Mallouk, T. E. *J. Phys. Chem. Lett.* **2011**, *2*, 402-406.

(17) Dismukes, G. C.; Brimblecombe, R.; Felton, G. A. N.; Pryadun, R. S.; Sheats, J. E.; Spiccia, L.; Swiegers, G. F. *Acc. Chem. Res.* **2009**, *42*, 1935-1943.
(18) McEvoy, J. P.; Brudvig, G. W. *Chem. Rev.* **2006**, *106*, 4455-4483.
(19) Artero, V.; Chavarot-Kerlidou, M.; Fontecave, M. *Angew. Chem. Int. Ed.* **2011**, *50*, 7238-7266.
(20) Li, F.; Zhang, B. B.; Li, X. N.; Jiang, Y.; Chen, L.; Li, Y. Q.; Sun, L. C. *Angew. Chem. Int. Ed.* **2011**, *50*, 12276-12279.
(21) Barber, J. *Chem. Soc. Rev.* **2009**, *38*, 185-196.
(22) Ferreira, K. N.; Iverson, T. M.; Maghlaoui, K.; Barber, J.; Iwata, S. *Science* **2003**, *303*, 1831-1838.
(23) Najafpour, M. M.; Heidari, S.; Amini, E.; Khatamian, M.; Carpentier, R.; Allakhverdiev, S. I. *J. Photoch. Photobio. B.* **2014**, *133*, 124-139.
(24) Tamaura, Y.; Kojima, M.; Sano, T.; Ueda, Y.; Hasegawa, N.; Tsuji, M. *Int. J. Hydrogen Energy* **1998**, *23*, 1185-1191.
(25) Tagore, R.; Crabtree, R. H.; Brudvig, G. W. *Inorg. Chem.* **2008**, *47*, 1815-1823.
(26) Kanan, M. W.; Nocera, D. G. *Science* **2008**, *321*, 1072-1075.
(27) Zhong, D. K.; Sun, J. W.; Inumaru, H.; Gamelin, D. R. *J. Am. Chem. Soc.* **2009**, *131*, 6086-6087.
(28) Han, A.; Wu, H.; Sun, Z.; Jia, H.; Yan, Z.; Ma, H.; Liu, X.; Du, P. *ACS Appl. Mater. Interfaces* **2014**, *6*, 10929-10934.
(29) Liang, Y. Y.; Wang, H. L.; Diao, P.; Chang, W.; Hong, G. S.; Li, Y. G.; Gong, M.; Xie, L. M.; Zhou, J. G.; Wang, J.; Regier, T. Z.; Wei, F.; Dai, H. J. *J. Am. Chem. Soc.* **2012**, *134*, 15849-15857.
(30) Eckenhoff, W. T.; McNamara, W. R.; Du, P.; Eisenberg, R. *Biochim. Biophys. Acta, Bioenerg.* **2013**, *1827*, 958-973.
(31) Dinca, M.; Surendranath, Y.; Nocera, D. G. *Proc. Natl. Acad. Sci. U.S.A.* **2010**, *107*, 10337-10341.
(32) Liu, X.; Jia, H.; Sun, Z.; Chen, H.; Xu, P.; Du, P. *Electrochem. Commun.* **2014**, *46*, 1-4.
(33) Gong, M.; Li, Y. G.; Wang, H. L.; Liang, Y. Y.; Wu, J. Z.; Zhou, J. G.; Wang, J.; Regier, T.; Wei, F.; Dai, H. J. *J. Am. Chem. Soc.* **2013**, *135*, 8452-8455.
(34) Chemelewski, W. D.; Lee, H. C.; Lin, J. F.; Bard, A. J.; Mullins, C. B. *J. Am. Chem. Soc.* **2014**, *136*, 2843-2850.
(35) Cook, T. R.; Dogutan, D. K.; Reece, S. Y.; Surendranath, Y.; Teets, T. S.; Nocera, D. G. *Chem. Rev.* **2010**, *110*, 6474-6502.
(36) Liu, X.; Chang, Z.; Luo, L.; Xu, T.; Lei, X.; Liu, J.; Sun, X. *Chem. Mater.* **2014**, *26*, 1889-1895.
(37) Cao, X.; Jin, C.; Lu, F.; Yang, Z.; Shen, M.; Yang, R. *J. Electrochem. Soc.* **2014**, *161*, H296-H300.
(38) Hou, X.; Wang, X.; Liu, B.; Wang, Q.; Luo, T.; Chen, D.; Shen, G. *Nanoscale* **2014**, *6*, 8858-8864.
(39) Ren, Z.; Botu, V.; Wang, S.; Meng, Y.; Song, W.; Guo, Y.; Ramprasad, R.; Suib, S.; Gao, P. *Angew. Chem. Int. Ed.* **2014**, *53*, 7223-7227.
(40) Chen, S.; Qiao, S.-Z. *ACS Nano* **2013**, *7*, 10190-10196.

(41) Li, Y.; Hasin, P.; Wu, Y. *Adv. Mater.* **2010**, *22*, 1926-1929.
(42) Cobo, S.; Heidkamp, J.; Jacques, P. A.; Fize, J.; Fourmond, V.; Guetaz, L.; Jousselme, B.; Ivanova, V.; Dau, H.; Palacin, S.; Fontecave, M.; Artero, V. *Nat. Mater.* **2012**, *11*, 802-807.
(43) Hove, M. A. V.; Somorjai, G. A. *Surf. Sci.* **1980**, *92*, 489-518.
(44) Mansour, A. N.; Melendres, C. A.; Pankuch, M.; Brizzolara, R. A. *J. Electrochem. Soc.* **1994**, *141*, L69-L71.
(45) Kim, J. G.; Pugmire, D. L.; Battaglia, D.; Langell, M. A. *Appl. Surf. Sci.* **2000**, *165*, 70-84.
(46) Li, J. G.; Buechel, R.; Isobe, M.; Mori, T.; Ishigaki, T. *J. Phys. Chem. C* **2009**, *113*, 8009-8015.
(47) Liang, Y. Q.; Cui, Z. D.; Zhu, S. L.; Li, Z. Y.; Yang, X. J.; Chen, Y. J.; Ma, J. M. *Nanoscale* **2013**, *5*, 10916-10926.
(48) Marco, J. F.; Gancedo, J. R.; Gracia, M.; Gautier, J. L.; Ríos, E.; Berry, F. J. *J. Solid State Chem.* **2000**, *153*, 74-81.
(49) Zhao, Y.; Nakamura, R.; Kamiya, K.; Nakanishi, S.; Hashimoto, K. *Nat. Commun.* **2013**, *4*.
(50) Liang, Y. Y.; Li, Y. G.; Wang, H. L.; Zhou, J. G.; Wang, J.; Regier, T.; Dai, H. J. *Nat. Mater.* **2011**, *10*, 780-786.
(51) Gao, M. R.; Xu, Y. F.; Jiang, J.; Zheng, Y. R.; Yu, S. H. *J. Am. Chem. Soc.* **2012**, *134*, 2930-2933.
(52) Perdew, J. P.; Chevary, J. A.; Vosko, S. H.; Jackson, K. A.; Pederson, M. R.; Singh, D. J.; Fiolhais, C. *Phys. Rev. B* **1992**, *46*, 6671-6687.
(53) Somorjai, G. A.; Blakely, D. W. *Nature* **1975**, *258*, 580-583.

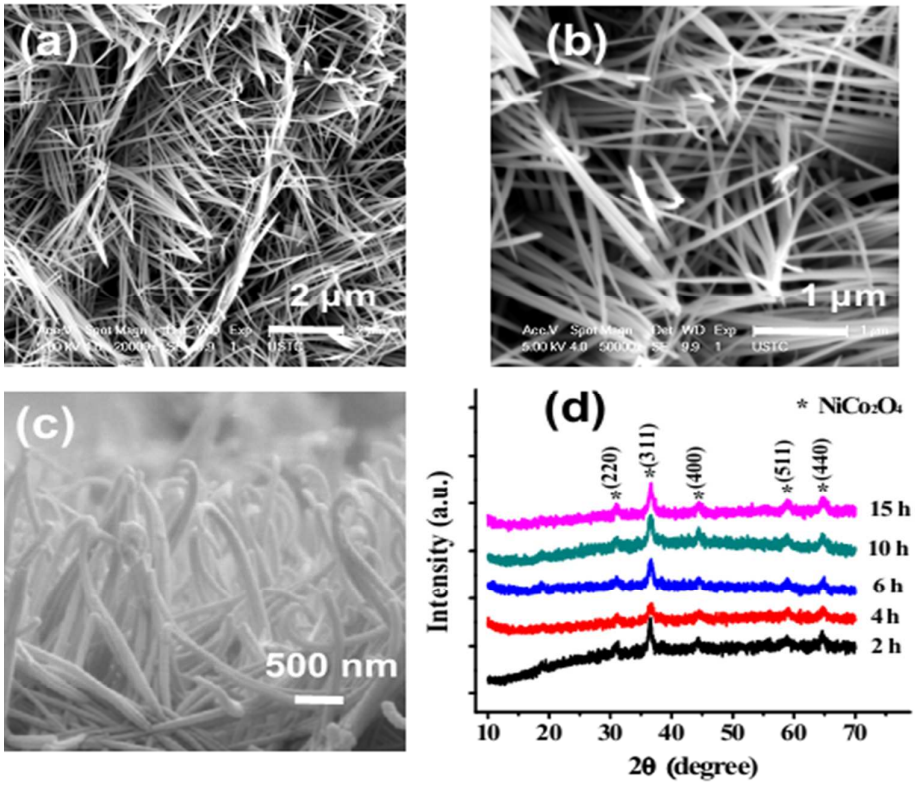

Figure 1. (a, b) SEM images of the $NiCo_2O_4$ after calcining at 350 ºC for 2 hours in flowing argon with 10 hours in hydrothermal synthesis at 120 ºC. (c) fracture surface of $NiCo_2O_4$ nanowire arrays. (d) XRD patterns of the $NiCo_2O_4$ obtained with different times in hydrothermal synthesis at 120 ºC.

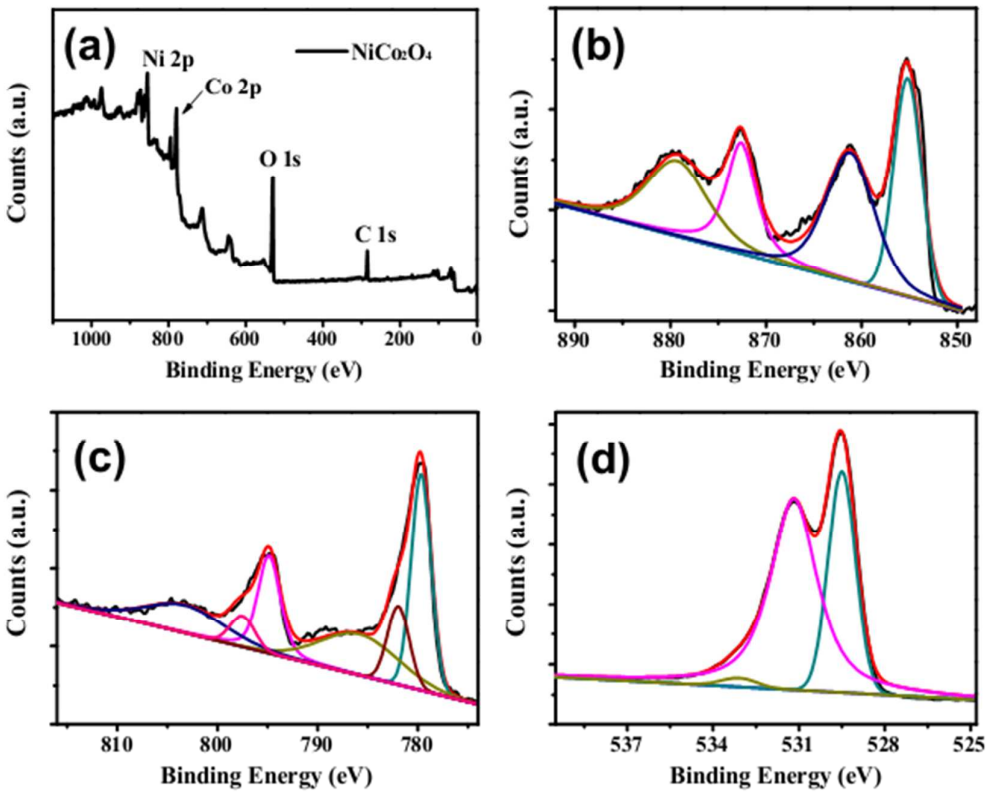

Figure 2. (a) XPS survey spectrum of the $NiCo_2O_4$ obtained by hydrothermal synthesis at 120 ºC for 10 hours; High resolution XPS spectra of (b) Ni 2p, (c) Co 2p, and (d) O 1s.

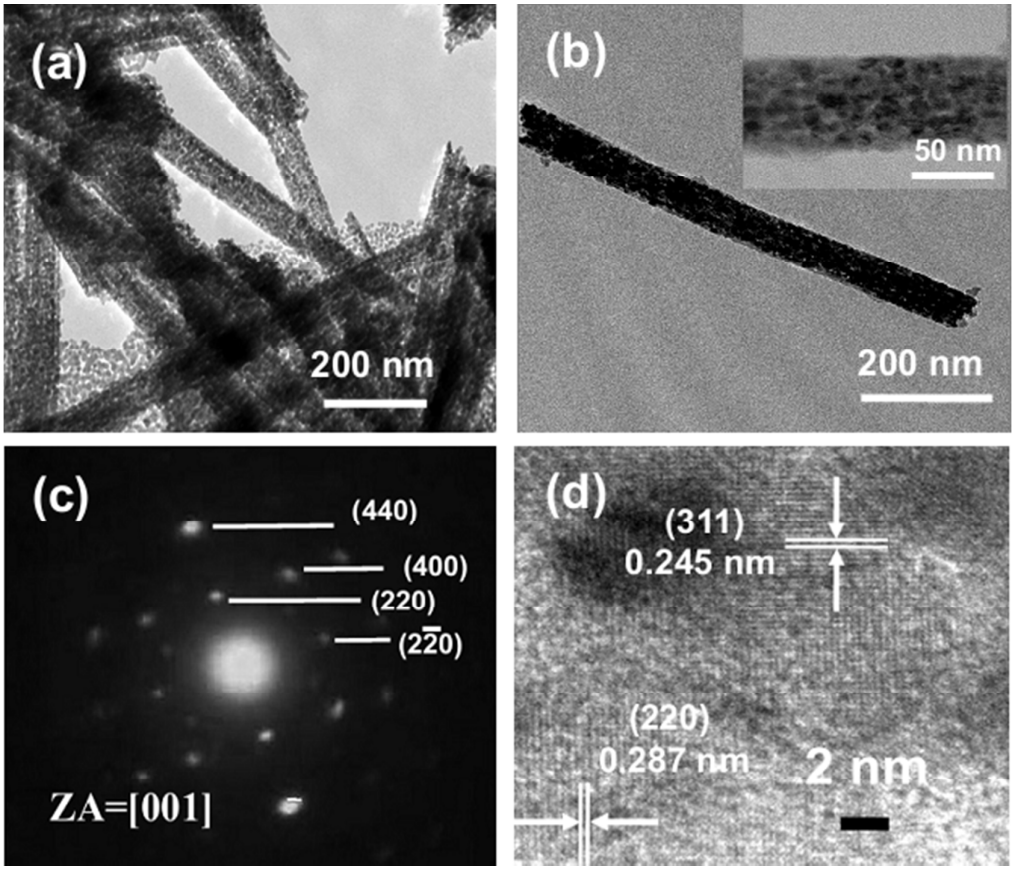

Figure 3. (a, b) TEM images of the $NiCo_2O_4$ nanowire arrays. (c) SAED analysis. (d) HRTEM images.

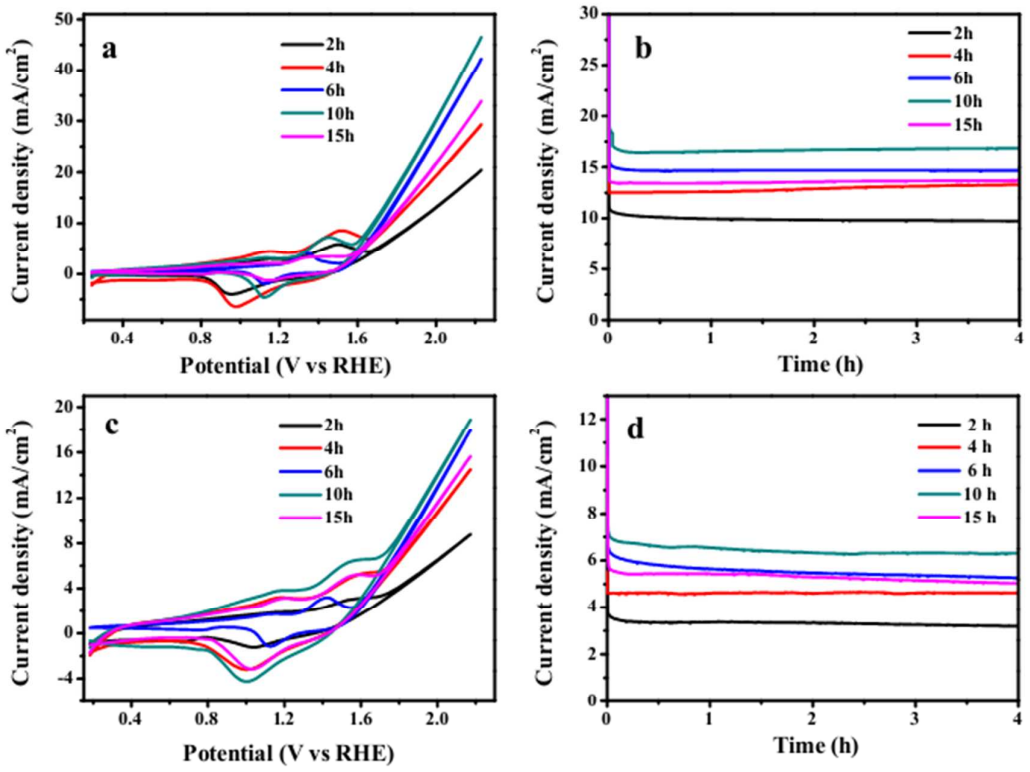

Figure 4. Electrochemical performance of $NiCo_2O_4$ nanoflakes and nanowires for different times in hydrothermal synthesis at 120 ºC as the working electrode in 1 M KOH or 0.1 M KOH. (a,c) CV curves, at 5 mV/s and with iR compensation in 1 M KOH or 0.1 M KOH. (b) Current density curves for bulk electrolysis at 1.83 V (an overpotential of 0.60 V) in 1 M KOH. (d) Current density curves for bulk electrolysis at 1.78 V (an overpotential of 0.55 V) in 0.1 M KOH.

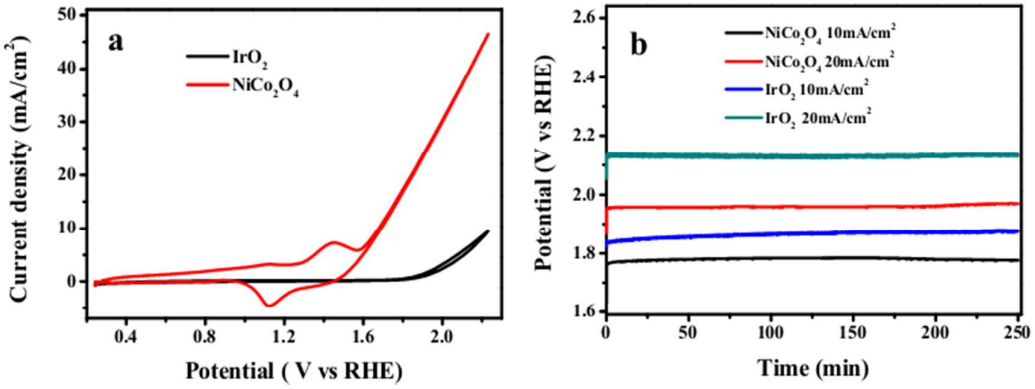

Figure 5. Electrochemical performance of $NiCo_2O_4$ NWAs at 120 ºC for 10 hours and IrO_2 (~1.0 mg/cm^2), as the working electrode in 1 M KOH. (a) CV curves of $NiCo_2O_4$ nanowires and IrO_2, at 5 mV/s and with iR compensation. (b) Chronopotentiometry curves of $NiCo_2O_4$ nanowires and IrO_2 under current densities of 10 and 20 mA/cm^2.

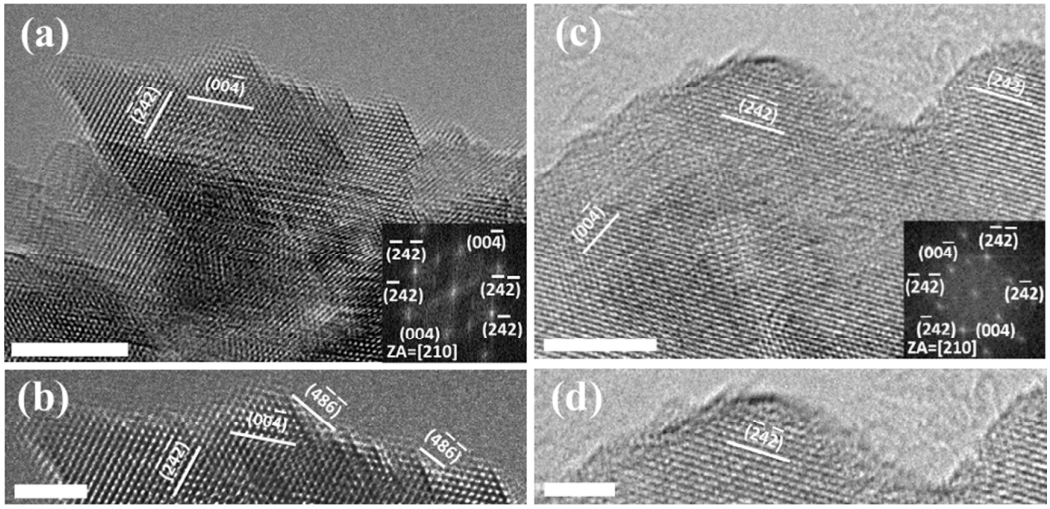

Figure 6. The HRTEM of the $NiCo_2O_4$ nanowires and nanoflakes. (a) The nanowire surface is composed of atomic steps. The inset of the (a) is the FFT pattern. The zone axis is along [210] direction. (b) The high-index facet $(2\bar{4}\bar{6})$ was observed on the surface, which plays important role on the catalytic performance. (c) and (d) The smooth surface of the nanoflakes. The inset of the (c) is the FFT pattern. The zone axis is along [210] direction. The scale bar is 5 nm in (a), (c) and 2.5 nm in (b), (d).

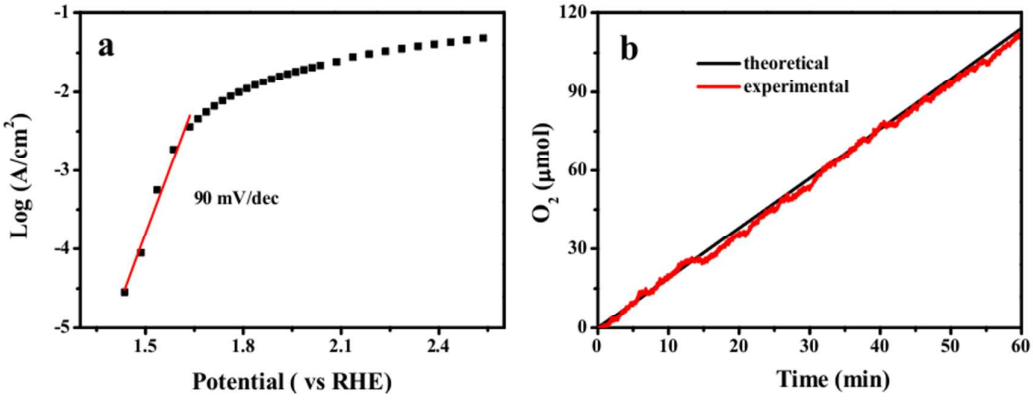

Figure 7. (a) Dependence of the current density on the potential in a 1 M KOH aqueous solution. The slope of the line is 90 mV per decade. (b) O_2 production measured by a fluorescence-based oxygen sensor and the theoretical amount of O_2 produced by electric charge transferred to water at 1.83 V in a 1 M KOH, corresponding to a Faradic efficiency of nearly 100%.

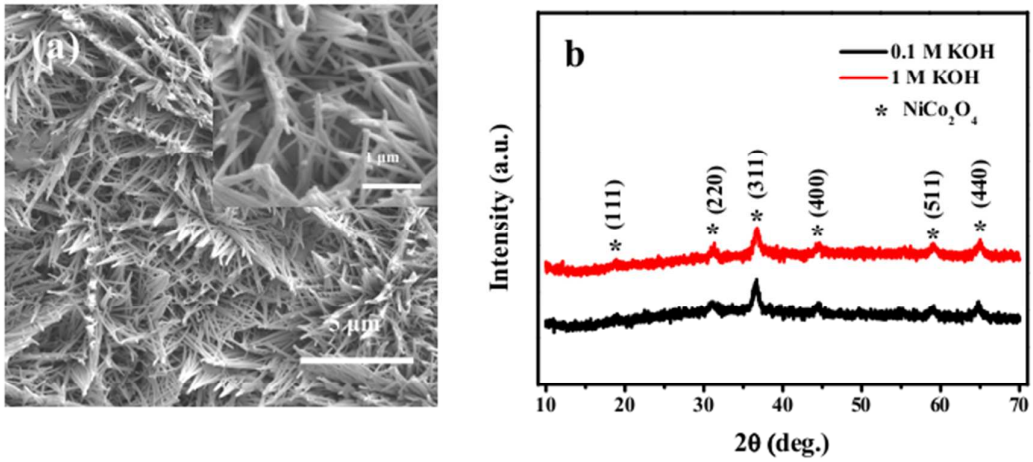

Figure 8. (a) SEM image of $NiCo_2O_4$ NWAs after >10 hours of electrolysis at 1.83 V in 1 M KOH. (b) XRD patterns of the $NiCo_2O_4$ NWAs after >10 hours of electrolysis at 1.78 V in 0.1 M KOH or at 1.83 V in 1 M KOH.

Table of Contents (TOC)